

Title: Ocean model response to stochastically perturbed momentum fluxes

Authors:

Terence J. O’Kane

CSIRO Oceans and Atmosphere, Hobart, Tasmania, Australia

terence.okane@csiro.au

Russell Fiedler

CSIRO Oceans and Atmosphere, Hobart, Tasmania, Australia

russell.fiedler@csiro.au

Mark A. Collier

CSIRO Oceans and Atmosphere, Aspendale, Victoria, Australia

mark.collier@csiro.au

Vassili Kitsios

CSIRO Oceans and Atmosphere, Aspendale, Victoria, Australia

Laboratory for Turbulence Research in Aerospace and Combustion, Department of Mechanical and Aerospace Engineering Monash University, Clayton, Victoria 3800, Australia

vassili.kitsios@csiro.au

This is a *non-peer reviewed preprint submitted to EarthArXiv.*

The preprint has been submitted to the AMS Journal of Climate for peer review.

1 **Ocean model response to stochastically perturbed momentum fluxes**

2 Terence J. O’Kane,^a Russell Fiedler,^a Mark A. Collier,^b Vassili Kitsios,^{b,c}

3 ^a *CSIRO Oceans and Atmosphere, Hobart, Tasmania, Australia*

4 ^b *CSIRO Oceans and Atmosphere, Aspendale, Victoria, Australia*

5 ^c *Laboratory for Turbulence Research in Aerospace and Combustion, Department of Mechanical*
6 *and Aerospace Engineering Monash University, Clayton, Victoria 3800, Australia*

7 *Corresponding author:* Terence J. O’Kane, terence.okane@csiro.au

8 ABSTRACT: In climate model configurations, standard approaches to the representation of un-
9 resolved, or subgrid scales, via deterministic closure schemes are being challenged by stochastic
10 approaches inspired by statistical dynamical theory. Despite gaining popularity, studies of various
11 stochastic subgrid scale parameterizations applied to atmospheric climate and weather prediction
12 systems have revealed a diversity of model responses, including degeneracy in the response to
13 different forcings and compensating model errors, with little reduction in artificial damping of the
14 small scales required for numerical stability. Due to the greater range of spatio-temporal scales
15 involved, how to best sample subgrid fluctuations in a computationally inexpensive manner, with
16 the aim of reduced model error and improvements to the simulated climatological state of the
17 ocean, remains an open question. While previous studies have considered perturbations to the
18 surface forcing or subsurface temperature tendencies, we implement an energetically consistent,
19 simple, stochastic subgrid eddy parameterization of the momentum fluxes in regions of the three-
20 dimensional ocean typically associated with high eddy variability. We consider the changes in
21 the modelled energetics of low-resolution simulations in response to stochastically forced velocity
22 tendencies whose perturbation statistics and amplitudes are calculated from an eddy resolving
23 ocean configuration. Kinetic energy spectra from a triple-decomposition reveal a systematic redis-
24 tribution from the seasonal (climatological minus mean) potential energy to preferentially generate
25 small scale transient kinetic energy while the total energy spectra remains largely unchanged.
26 We show that stochastic parameterization generally improves model biases, noticeably so for the
27 simulated energetics of the Southern Oceans.

28 **1. Introduction**

29 The question of how to incorporate the effects of unresolved turbulent motions, and their role
30 in determining large scale dynamics, represents a common problem in large eddy simulations
31 (LES) of nonlinear fluids and one that is particularly crucial for simulating geophysical flows.
32 In ocean and climate modelling it is typical to employ deterministic methods which, due to the
33 computational cost, often requires reduced resolution model configurations to enable long time
34 simulations whereby only the statistical effects of the subgrid scales (eddies) on the retained large
35 scales (mean flow) can be approximated empirically. Furthermore, it is well known that small scale
36 errors grow rapidly on (finite) timescales determined by their initial spatial structure, where even
37 small random errors will quickly become organised by the model dynamics and undergo rapid
38 growth and projection onto large scale mean features of the flow. The structure and growth rate of
39 small scale errors is not confined to subgrid parameterizations but to all aspects of simulating and
40 predicting geophysical flows (Kalnay 2003).

41 It has long been recognised that elements of the climate system might be represented by re-
42 duced order (linear) stochastic models, of which the principal oscillation or linear inverse model
43 (Hasselmann 1976) is a classical example with a long history of application to ocean dynamics
44 (Frankignoul and Hasselmann 1977; Penland 1989; Penland and Sardeshmukh 1995; Lou et al.
45 2021). More recently data driven approaches have been developed and applied for the construction
46 of nonstationary reduced order stochastic models (Metzner et al. 2012) of the atmosphere (Horenko
47 2010) allowing for the identification of persistent regime behaviour such as that associated with the
48 low frequency variability of the North Atlantic Oscillation (Quinn et al. 2021). These approaches
49 to modeling geophysical flows assume scale separation i.e., that only a subset of large scale modes
50 need to be resolved and that the subgrid scales may be represented in terms of stochastic noise
51 forcing.

52 A foundational understanding of subgrid parameterizations to correct biases in the small scale
53 energy spectra of LES has deep roots in statistical dynamics. As discussed by O’Kane and Fred-
54 eriksen (2008a), fundamental insights into stochastic-dynamic parameterization were pioneered
55 by the efforts of a key group working on turbulent energy closures for ensemble weather predic-
56 tion. Specifically, the work of Epstein (1969), Fleming (1971a,b) and Pitcher (1977) (see also
57 Epstein and Pitcher (1972)) in which third and higher order cumulants are discarded in order to

58 directly forecast mean and variance information via statistical dynamical prognostic equations and
59 stochastic perturbations to velocity tendencies. However, it was the seminal work of Kraichnan
60 (1976) that marked the arrival of the modern theory of eddy viscosity and stochastic backscatter
61 i.e. injection and or drain of energy with a predetermined renormalised functional form. Since
62 then, there have been ongoing efforts over several decades to establish a rigorous mathematical
63 basis for subgrid scale parameterizations based on statistical mechanics and dynamics, including
64 formal renormalization methods (Frederiksen 1999; O’Kane and Frederiksen 2008b), stochastic
65 approximations (Zidihkeri and Frederiksen 2008) and the subsequent identification of universal
66 scaling laws for subgrid dynamics in atmospheric and oceanic flows (Kitsios et al. 2016). For
67 a comprehensive review of the development of statistical dynamics and closures see the recent
68 review by Zhou (2021). Various approaches to incorporating stochastic kinetic energy backscatter
69 have for some time now been applied to reduce systematic model errors in operational weather
70 prediction and atmospheric climate models (Berner et al. 2012; Franzke et al. 2015; Berner and
71 coauthors 2017).

72 The aforementioned approaches seek to identify the scale dependent functional form of drain
73 and injection terms in order to correct the energy spectrum of the smallest resolved scales in LES.
74 One unavoidable consequence of the addition of stochastic forcing to a nonlinear system is that,
75 typically, the amplitude of the noise increases with wavenumber hence making the small scales
76 more isotropic and weakening phase relationships. In this case, whereas the energy spectrum may
77 be improved, structure is lost. Additionally, it is often unclear the spatio-temporal scales at which
78 the model will organise the noise and hence there is no a priori way to determine the coherent
79 response to the forcing. Simply put, it remains unclear as to how any given nonlinear dynamical
80 system will respond to a particular application of stochastic forcing.

81 Stochastic forcing can act in many ways to modify the dynamics of a nonlinear system. Examples
82 include regime transitions in simple scalar systems such as the stochastically forced double well
83 potential (Miller et al. 1985). In two-dimensional turbulence, weak stochastic forcing of a particular
84 large scale mode or particular small wavenumber has been shown to be able to initiate large energy
85 transfers from small to large scales via the inverse energy cascade (Bouchet and Simonnet 2009;
86 Nadiga and O’Kane 2017). More generally, it has for some time now been recognised that
87 stochastic forcing of the ocean surface fluxes, even isotropic random perturbations with zero mean,

88 interacting with nonlinearities in the (climate) model equations can lead to enhanced variability and
89 changes in the mean (climatological) state (Zavala-Garay et al. 2003; Beena and von Storch 2009;
90 Williams 2012). Williams et al. (2016) showed the response to zero mean multivariate stochastic
91 perturbations to the temperature tendencies in the three dimensional ocean. They considered
92 both isotropic uncorrelated and correlated noise forcing whose amplitude was calculated from a
93 $1/3^\circ$ horizontal resolution 40 vertical level climate ocean model to stochastically force the ocean
94 temperature tendencies of a very low resolution 2.5° latitude and 3.75° longitude, 20 vertical
95 level model. They found a stronger response occurred for correlated noise and with significant
96 warming of the upper ocean and cooling at depth such that an overall significant loss of global
97 ocean heat content occurred. Overall, they argue that perturbed temperature tendencies resulted
98 in reduced biases and improved ocean temperature and salinity fields both at the surface and at
99 depth, as well as improvements in the variability of the strength of the global ocean thermohaline
100 circulation. The choice to perturb temperature tendencies in the three dimensional ocean state
101 is consistent with well established reduced order models for examining ocean predictability (Lou
102 et al. 2021) and applications examining initialization for ensemble ocean forecasting based on
103 optimal perturbations to temperature (O’Kane et al. 2011). However, perturbing temperature alone
104 is potentially problematic for large density compensated regions of the ocean and is inconsistent
105 with energetics i.e. potential energy transfers of the form $u' \rho' \frac{\partial \rho}{\partial x}$.

106 O’Kane et al. (2013) showed that forcing of a low resolution Southern Ocean via the observed
107 synoptic scale anomalous surface winds alone could account for the majority of the simulated
108 variability in the subsurface Antarctic Circumpolar Current. Subsequently, O’Kane et al. (2014b)
109 showed that even very weak stochastic forcing of the ocean surface winds can lead to excitation
110 of chaotic oscillations in temperature and salinity in a low resolution ocean model, particularly
111 in regions typically associated with tropical instability waves and subtropical baroclinic Rossby
112 waves (O’Kane et al. 2014a; Chapman et al. 2020). However, there remains much uncertainty as
113 to how best to apply, or even whether to apply, stochastic forcing to the three-dimensional state of
114 a particular ocean or climate general circulation model (GCM) and what the modelled response
115 might be.

116 Here we apply stochastic perturbations to the horizontal momentum flux in a general circulation
117 ocean - sea ice model configuration with resolution typical for climate simulations. We argue that

118 direct stochastic forcing of the velocity tendencies is more consistent with statistical dynamical
119 theory and more aligned with applications in weather prediction. Specifically, a high resolution
120 $1/10^\circ$ eddy resolving reference calculation forced by nominal year surface boundary conditions is
121 used to determine regions of high eddy variance that are unresolved in the low resolution model
122 and to set the amplitude of the applied stochastic perturbations. A low resolution 1° control
123 simulation is first run to steady state, also forced by nominal year surface boundary conditions,
124 after which a series of simulations with stochastic perturbations to the horizontal momentum flux
125 are conducted. The perturbation amplitudes are applied as a fraction of the variance of the reference
126 eddy variability. A control simulation is run out to steady state (≈ 2000 years), then each of the
127 stochastically perturbed simulations are also run to steady state, which is achieved after ≈ 150 years,
128 and continued for another two decades. The final decade of each of the 170 year simulations was
129 used to examine the climatological (mean) ocean states, energetics and transports.

130 We describe the model configurations and construction of the stochastic forcing in section 2.
131 Results for a range of diagnostics are presented in section 3 followed by summary and discussion
132 in section 4.

133 **2. Experimental design and model configuration**

134 *a. Model configurations*

135 We employ the ACCESS-OM community model (Kiss et al. 2020) driven by JRA55-do repeat
136 year forcing (Stewart et al. 2020) at two horizontal resolutions i.e. nominally 1° and 0.1° . These
137 models have been configured with model parameters as consistent as possible to assist in studies
138 of resolution dependence. Away from the continental shelf and equatorward of 50° , the 0.1°
139 model resolves the first baroclinic deformation radius indicating some degree of representation of
140 a transient mesoscale eddy field, whereas the 1° does not. The low and high resolution models
141 have different vertical resolutions where the vertical grid in the ACCESS-OM2 1° configuration
142 has 50 levels and 2.3m spacing at the surface, increasing smoothly to 219.6m by the bottom at
143 5363.5 m, whereas the ACCESS-OM2 0.1° configuration has 75 levels and 1.1m spacing at the
144 surface, increasing smoothly to 198.4m by the bottom at 5808.7 m. Kiss et al. (2020) provide a
145 detailed description of the model parameters and performance of ACCESS-OM2 at three horizontal
146 resolutions i.e. 1° , 0.25° and 0.1° .

147 *b. Stochastic forcing*

148 Firstly, annual and seasonally varying climatological root mean squared errors (rmse) are cal-
 149 culated from the horizontal velocities using the final 10 years of a long control simulation of the
 150 ACCESS-OM 0.1° model. The rmse are limited to only those values exceeding 0.15 ms^{-1} then
 151 regrided to the ACCESS-OM 1° grid. The instantaneous zonal and meridional velocity tendencies
 152 $(\frac{\partial u}{\partial t}, \frac{\partial v}{\partial t})$ are then perturbed by the addition of a random fluctuation (ϵ_u, ϵ_v) uniformly distributed
 153 between $[-1, 1]$ with zero mean and scaled to be some fraction of the rmse of the ACCESS-OM
 154 0.1° model. In this way, the tensorial flux form of the momentum equations in a curvilinear
 155 z-coordinate system (Madec and the NEMO team 2016) are now given by

$$\begin{aligned} \frac{\partial u}{\partial t} = & \left(f + \frac{1}{e_1 e_2} \left(v \frac{\partial e_2}{\partial i} - u \frac{\partial e_1}{\partial j} \right) \right) v \\ & - \frac{1}{e_1 e_2} \left(\frac{\partial (e_2 u^2)}{\partial i} + \frac{\partial (e_1 v u)}{\partial j} \right) - \frac{1}{e_3} \frac{\partial (w u)}{\partial k} \\ & - \frac{1}{e_1} \frac{\partial}{\partial i} \left(\frac{p_s + p_h}{\rho_o} \right) + \epsilon_u + (\text{subgrid terms} + \text{surface forcing}) \end{aligned} \quad (1a)$$

$$\begin{aligned} \frac{\partial v}{\partial t} = & - \left(f + \frac{1}{e_1 e_2} \left(v \frac{\partial e_2}{\partial i} - u \frac{\partial e_1}{\partial j} \right) \right) u \\ & - \frac{1}{e_1 e_2} \left(\frac{\partial (e_2 u v)}{\partial i} + \frac{\partial (e_1 v^2)}{\partial j} \right) - \frac{1}{e_3} \frac{\partial (w v)}{\partial k} \\ & - \frac{1}{e_2} \frac{\partial}{\partial j} \left(\frac{p_s + p_h}{\rho_o} \right) + \epsilon_v + (\text{subgrid terms} + \text{surface forcing}) \end{aligned} \quad (1b)$$

156 where (i, j, k) are orthogonal curvilinear coordinates on the sphere associated with the positively
 157 oriented orthogonal set of unit vectors $(\mathbf{i}, \mathbf{j}, \mathbf{k})$ such that \mathbf{k} is the local upward vector and (\mathbf{i}, \mathbf{j}) are
 158 two vectors orthogonal to \mathbf{k} along geopotential surfaces. Here (λ, φ, z) define the geographical
 159 coordinate system where position is defined by the latitude $\varphi(i, j)$, the longitude $\lambda(i, j)$ and the
 160 distance from the centre of the earth $a + z(k)$ and where a is the earth's radius and z the altitude
 161 above a reference sea level. The local deformation of the curvilinear coordinate system is then

180 TABLE 1. Model configuration and amplitude of stochastic forcing as a percentage of the standard deviation
 181 from the ACCESS-OM2-0.1 high resolution reference simulation.

Model	resolution	amplitude
ACCESS-OM2-0.1	1/10°	0
ACCESS-OM2-1 (control)	1°	0
stochastic-1	1°	10%
stochastic-2	1°	20%
stochastic-5	1°	50%
stochastic-10	1°	100%

162 given by e_1 , e_2 and e_3 , three scale factors defined as

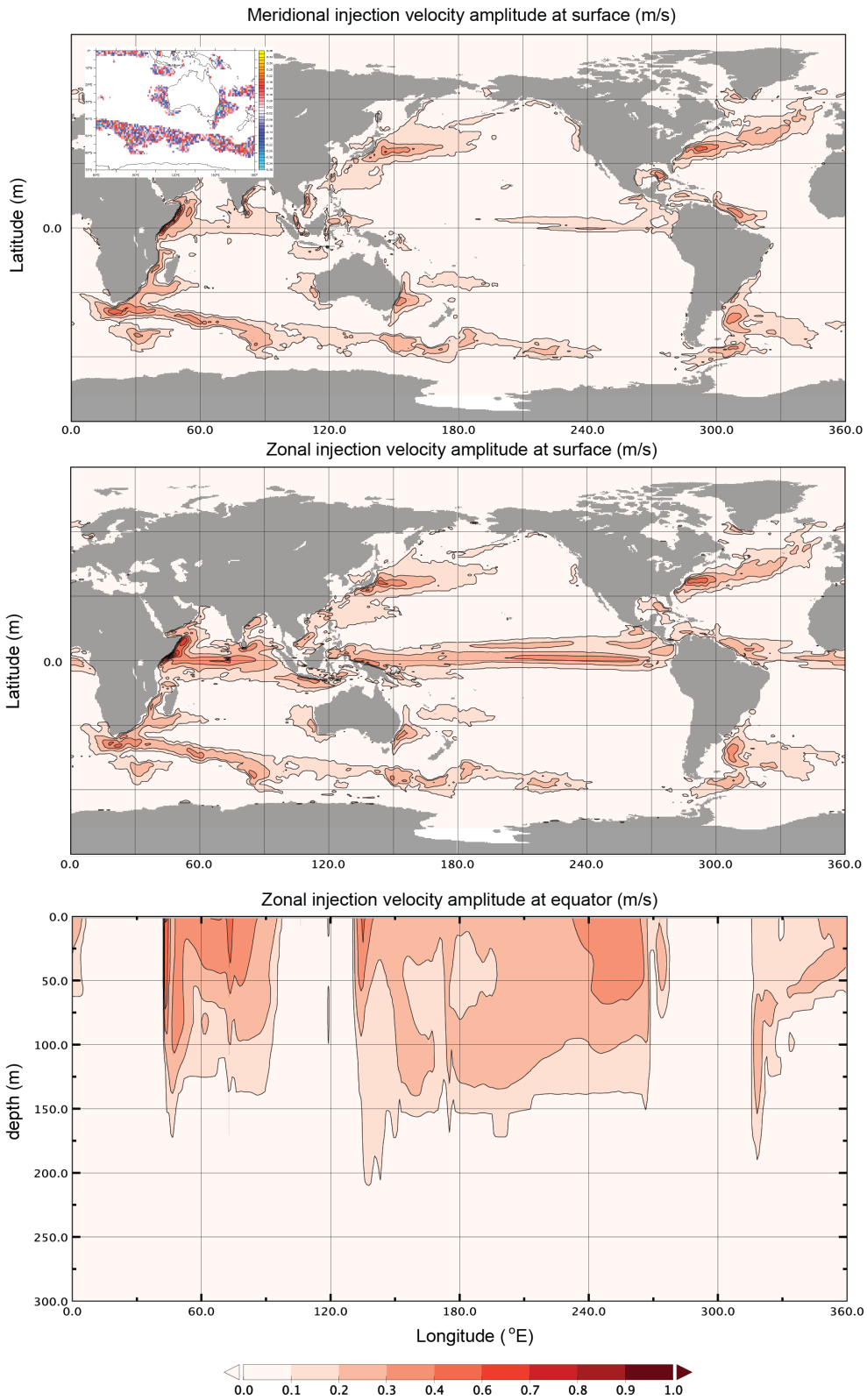
$$e_1 = (a + z) \left[\left(\frac{\partial \lambda}{\partial i} \cos \phi \right)^2 + \left(\frac{\partial \phi}{\partial i} \right)^2 \right]^{1/2} \quad (2a)$$

$$e_2 = (a + z) \left[\left(\frac{\partial \lambda}{\partial j} \cos \phi \right)^2 + \left(\frac{\partial \phi}{\partial j} \right)^2 \right]^{1/2} \quad (2b)$$

$$e_3 = \left(\frac{\partial z}{\partial k} \right) \quad (2c)$$

166 The masks are three dimensional with surface values of the zonal and meridional injection velocity
 167 amplitudes shown in figures 1a & b. Specifically, we show the amplitude (mean) for the meridional
 168 and zonal velocity tendency forcing at the surface and also for the zonal velocities down to 300m
 169 depth along the equator (figure 1c). The inset in figure 1a) illustrates the stochastic forcing on
 170 the meridional velocity tendency at a particular instant after regridding. The stochastic forcing is
 171 applied at each model timestep.

172 In the experiments that follow we consider stochastic forcing strengths of 10%, 20%, 50% and
 173 100% of the regridded 0.1° amplitude RMSE of anomalies with respect to climatology on the
 174 tendencies, and compared to a control simulations of the 1° model and a reference 0.1° model
 175 simulation as described in table 1. We further note that the decorrelation timescales for the
 176 velocities are significantly shorter than for temperature which is an important difference between
 177 this experimental design and that of earlier works where only temperature tendencies were perturbed
 178 (Williams et al. 2016) or where SST perturbations have been directly applied to analysed states
 179 (Andrejczuk et al. 2016).



163 FIG. 1. Masks for stochastic perturbations to the velocity tendencies. The inset into the top panel shows the
 164 spatial distribution of instantaneous random values distributed between $[-1, 1]$ within the mask about Australia
 165 and the Southern Ocean.

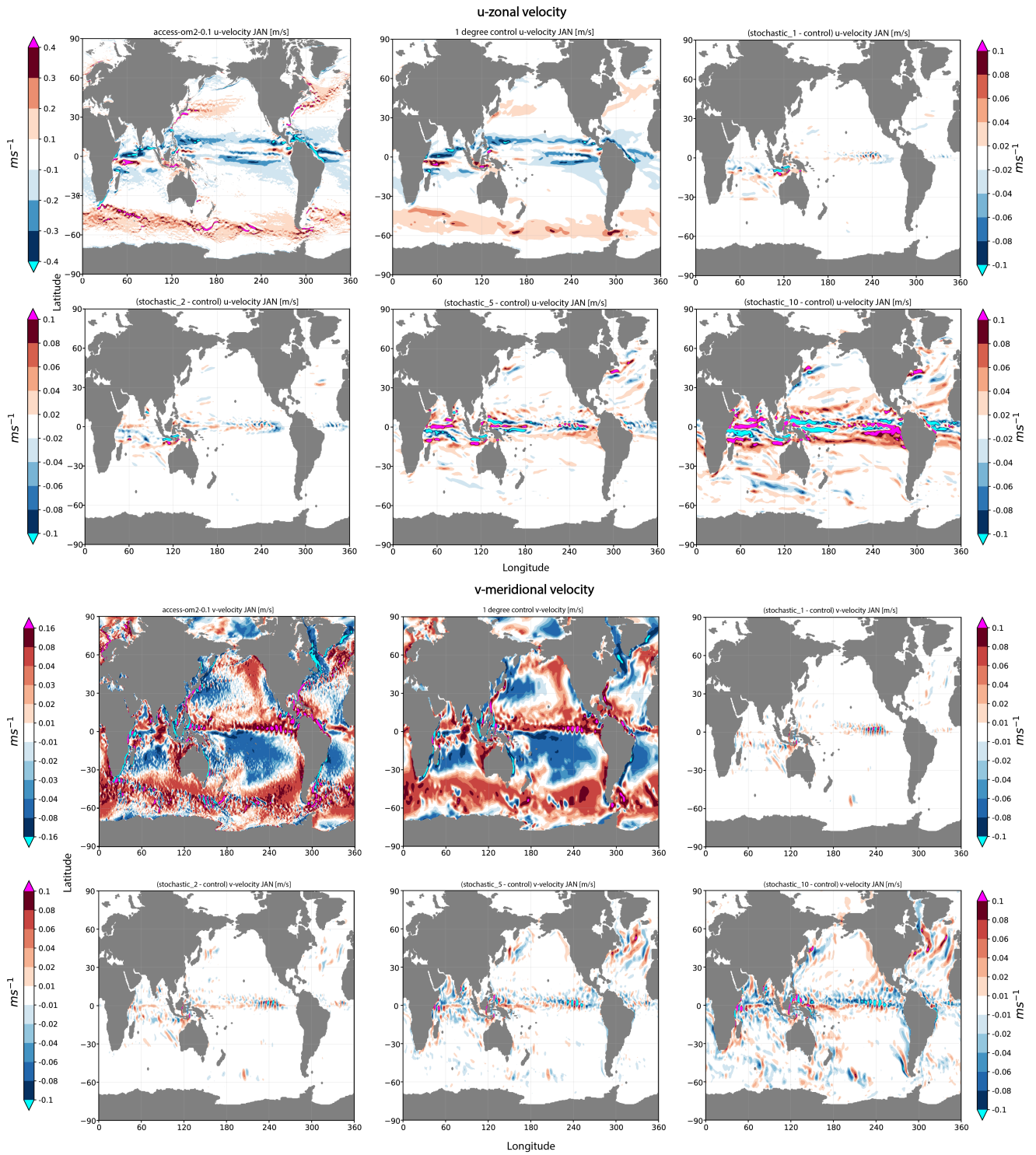
182 **3. Results**

183 *a. Velocities*

186 In figures 2 we show the surface zonal and meridional velocity averaged over each January of the
187 last decade of the respective 170 year simulations with JRA55-do repeat year forcing applied. All
188 1° model simulations have started from the same initial conditions and all anomalies are relative to
189 each respective model climatology calculated over a period where models are very close to steady
190 state. In addition to an unperturbed control simulation (upper middle panels), we also include a
191 0.1° reference simulation ACCESS-OM2-0.1 (upper left panel). The remaining panels in figures 2
192 show differences between the respective stochastically perturbed and control 1° simulations.

193 Of immediate note for the zonal velocities, is the good correspondence between the broad features
194 of the high resolution reference and low resolution control simulations. This is expected, given
195 both models are driven with the same surface forcing. Also to be expected, is the absence of
196 high amplitude, small scale features in the low resolution control simulation, and in particular
197 in the Antarctic Circumpolar Current (ACC) and in the midlatitude boundary current regions
198 such as the Kuroshio and Gulf Stream. In comparison to the ACCESS-OM2-1 control, it is the
199 tropics, and in particular the Indonesian Through Flow (ITF) and Indian Ocean that respond most
200 immediately to the applied stochastic forcing. The responses seen in the 10% stochastic-1 and
201 20% stochastic-2 simulations are in the tropical instability waves in the equatorial Pacific and
202 Atlantic, an equatorward displacement of the current associated with the ITF and similarly with
203 the Indian ocean storm track extending from the Western Australian coast (O’Kane et al. 2014a;
204 Chapman et al. 2020). As the amplitude of the perturbations is increased, we continue to see a
205 strong response in the tropics but also responses in the Kuroshio and Gulf Stream associated with
206 a poleward displacement of their separation and extensions.

207 For the meridional velocity there is a similar close correspondence between the broad scale
208 structures of the respective high resolution reference and low resolution control simulations. There
209 is a strong response in the equatorial Pacific at 240° longitude, evident for even very weak stochastic
210 forcing. This region has been previously identified by O’Kane et al. (2014b) to be characterised
211 by high intrinsic variability and a strong sensitivity to stochastic atmospheric forcing. As the
212 strength of the perturbation amplitude is increased there emerges responses at the midlatitudes



184 FIG. 2. High and low resolution zonal and meridional surface velocities averaged over last decade of 170 year
 185 simulation and differences between stochastic and control simulations.

213 and in particular located wherever major topographic features are present. For example, in the
 214 Southern Ocean in the ACC we see significant shifts in the meridional velocities in the vicinity of
 215 the East Pacific Rise. This region has previously been noted as one where intrinsic variability can
 216 be excited by reanalysed synoptics scale atmospheric surface (10 meter) winds alone (O’Kane et al.
 217 2013). In the northern hemisphere, for the higher amplitude perturbations, there are significant
 218 responses across the entire North Atlantic and a westward shift in the Kuroshio separation.

219 *b. Energy*

220 The primary reason to perturb the velocity tendencies is to modify the momentum flux and the
 221 energetics. The total energy tendency (Orlanski and Cox 1973; Oey 2007) can be written as

$$\frac{d}{dt} (EKE + EPE) = -\nabla \cdot (\overline{\mathbf{v}'p'}/\rho_0) + BT + BC + KH \quad (3a)$$

222 Here

$$EKE = \frac{1}{2} (\overline{u'^2} + \overline{v'^2}) \quad (3b)$$

$$EPE = \frac{g^2}{2N^2} \frac{\overline{\rho'}}{\rho_0^2} \quad (3c)$$

$$BT = -\left(\overline{u'^2} \frac{\partial \overline{u}}{\partial x} + \overline{v'^2} \frac{\partial \overline{v}}{\partial y} + \overline{u'v'} \frac{\partial \overline{u}}{\partial y} + \overline{u'v'} \frac{\partial \overline{v}}{\partial x} \right) \quad (3d)$$

$$BC = -\frac{g^2}{\rho_0^2 N^2} \left(\overline{u'\rho'} \frac{\partial \overline{\rho}}{\partial x} + \overline{v'\rho'} \frac{\partial \overline{\rho}}{\partial y} \right) \quad (3e)$$

$$KH = -\left(\overline{w'u'} \frac{\partial \overline{u}}{\partial z} + \overline{w'v'} \frac{\partial \overline{v}}{\partial z} \right) \quad (3f)$$

223 where ρ is the density of sea water, p the pressure, and N^2 the buoyancy frequency. In general
 224 the overline i.e. \overline{u} , can refer to the time mean but here will indicate the monthly climatology with
 225 primes i.e. u' , denoting anomalies about the climatology. For the respective terms in Eqn. 3a,
 226 EKE is the transient or eddy kinetic energy and EPE the transient potential energy; BT and BC
 227 are the barotropic and baroclinic conversion terms. For BT positive, energy is drained from the
 228 mean horizontal shears to the eddy field whereas; for BC positive, energy is drained from the
 229 horizontal density gradients, equivalent to the mean available potential energy, to the eddy field.

230 Contributions from the mean vertical shears and Reynolds stresses in the vertical plane are included
 231 in the Kelvin–Helmholtz (KH) instability. In order for conservation of energy transfers, release of
 232 mean kinetic energy (i.e. positive BT and KH) must be accompanied by capture of potential energy
 233 (i.e. negative BC). The divergence (i.e., pressure work) term $-\nabla \cdot (\overline{\mathbf{v}'p'}/\rho_0)$ vanishes if integrated
 234 over a closed domain. We can define an additional exchange term, that, if positive, describes the
 235 drain of energy from EPE into EKE

$$PKC = -\frac{g}{\rho_0}(\overline{\rho'w'}). \quad (4)$$

236 In the results to follow, due to the negligible changes to the vertical velocities w in the experiments
 237 with stochastic forcing of the horizontal velocity tendencies, KH contributions will not be explicitly
 238 considered.

239 Following Oliver et al. (2015), we consider the time mean transient (eddy) kinetic energy EKE
 240 in Joules (J) within a volume V in the modified form

$$EKE = \frac{1}{2} \int_V \rho(\overline{u'^2} + \overline{v'^2}) dV. \quad (5)$$

241 Following O’Kane et al. (2013), the transfer rate of mean to transient potential energy representing
 242 baroclinic instabilities, in Joules per second (J/s), is now given by

$$GPE = g \int_V \frac{\overline{u'\rho' \frac{\partial \tilde{\rho}}{\partial x}} + \overline{v'\rho' \frac{\partial \tilde{\rho}}{\partial y}}}{\frac{\partial \tilde{\rho}}{\partial z}} dV \quad (6)$$

243 where g is the acceleration due to gravity and $\tilde{\rho}$ is a reference state for the ocean approximated by
 244 the zonally and meridionally averaged density.

245 1) TIMESERIES

246 We first consider the global volume integrated, annual averages of the kinetic and potential
 247 energy and temperature (figure 3). The transient kinetic energy is determined by the anomalous
 248 velocities and, after a dramatic increase over the first decade, attains stable values after year 50.
 249 The values of the response of the model to increasing amplitude of the perturbations is not quite
 250 linear with global values of approximately $7 \times 1e^{17}$ J for the control and $17 \times 1e^{17}$ J for the stochastic-

251 10 simulation. For the potential energy, we see significant reductions of up to 8% and 30% for
 252 the simulations with the 50% (stochastic-5) and 100% (stochastic-10) amplitude perturbations.
 253 There is also a corresponding increase in global volume annual averages of ocean temperature
 254 such that at year 170, there are increases of approximately 4% and 12% for the stochastic-5 and
 255 stochastic-10 simulations respectively, relative to the initial state. The increase in mean kinetic
 256 energy accompanied by decreasing potential energy is consistent with the earlier discussion of the
 257 energetics.

258 2) KINETIC ENERGY SPECTRA

259 The question arises as to the mechanism by which the energetics and temperature in the model
 260 respond to increasingly larger amplitude stochastic perturbations. As the stochastic forcing applied
 261 to the velocity tendencies has zero mean, we expect that energy is being redistributed across scales
 262 and not injected. The application of stochastic forcing to redistribute energy across disparate scales,
 263 with corresponding modifications to large scale flow structures, has been examined previously in
 264 the context of two-dimensional turbulence (Bouchet and Simonnet 2009; Loxley and Nadiga 2013;
 265 Nadiga and O’Kane 2017) but not to our knowledge for an ocean GCM. To better understand the
 266 redistribution of energy and the source of the increased transients in our low resolution ocean
 267 GCM, we next consider the kinetic energy spectra averaged across the global ocean. Specifically
 268 we consider total KE and its component parts in terms of the triple decomposition (Hussain and
 269 Reynolds 1970; Kitsios et al. 2010)

$$\zeta(x, t) = \langle \zeta(x) \rangle + \tilde{\zeta}(x, t) + \zeta'(x, t) \quad (7)$$

270 i.e. $\bar{\zeta}(x) = \langle \zeta(x) \rangle + \tilde{\zeta}(x, t)$ (climatology); $\tilde{\zeta}(x, t)$ (seasonal = climatology minus mean); $\zeta'(x, t)$
 271 (anomalies about the climatology); where the mean $\langle \zeta(x) \rangle = \frac{1}{T} \int_0^T \zeta(x, t) dt$ with T the length of
 272 the timeseries.

273 In the top row of figure 4 we show the total KE and its constituent components i.e. mean, seasonal
 274 and anomalous KE. We show spectra calculated from velocities depth averaged to 1000m, noting
 275 that investigations at various depth levels in the upper ocean reveal a qualitatively similar picture.
 276 The total and mean KE spectra are closely matched for the control and all stochastically forced
 277 models indicating that the total energy remains largely conserved regardless of the strength of the

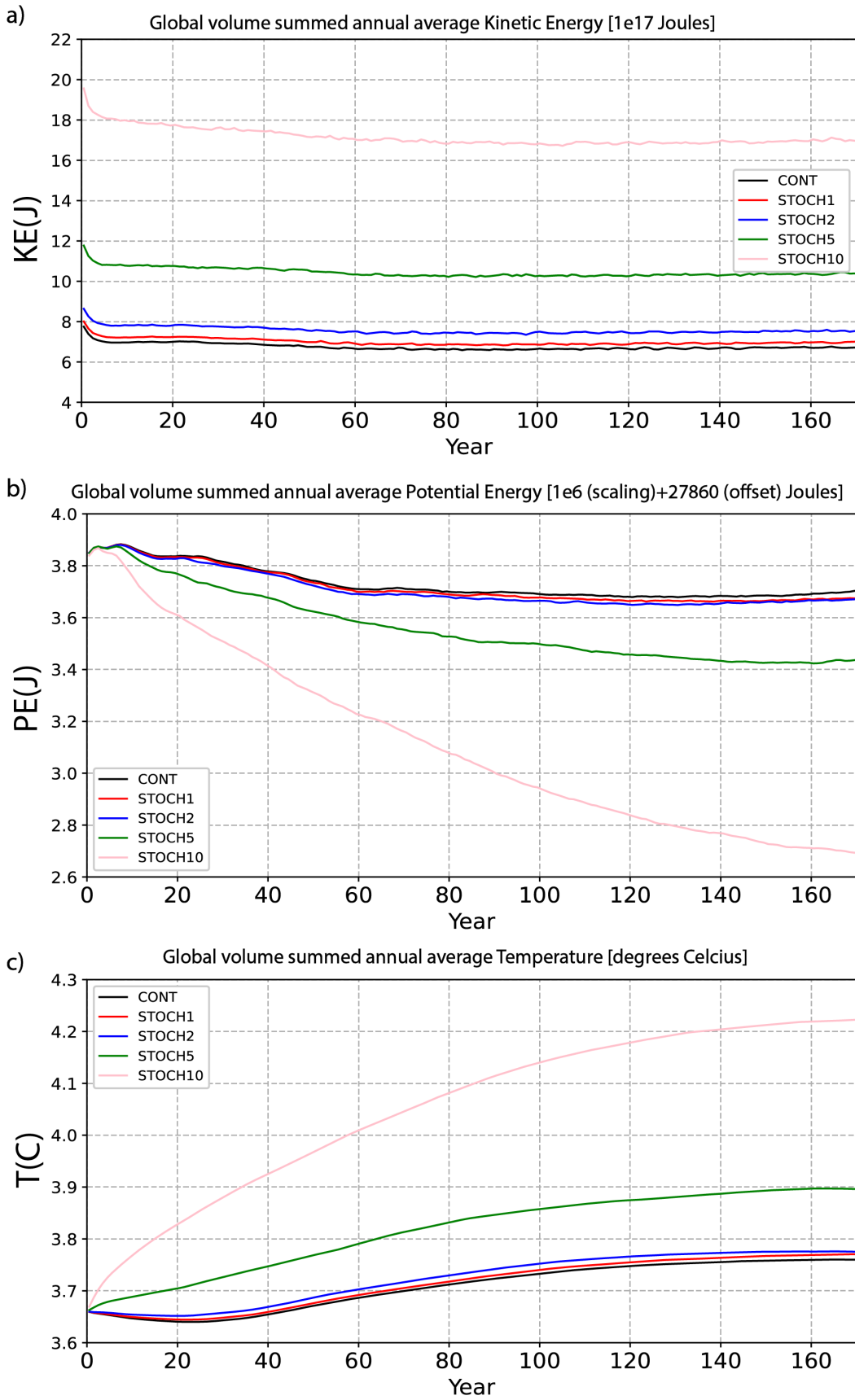


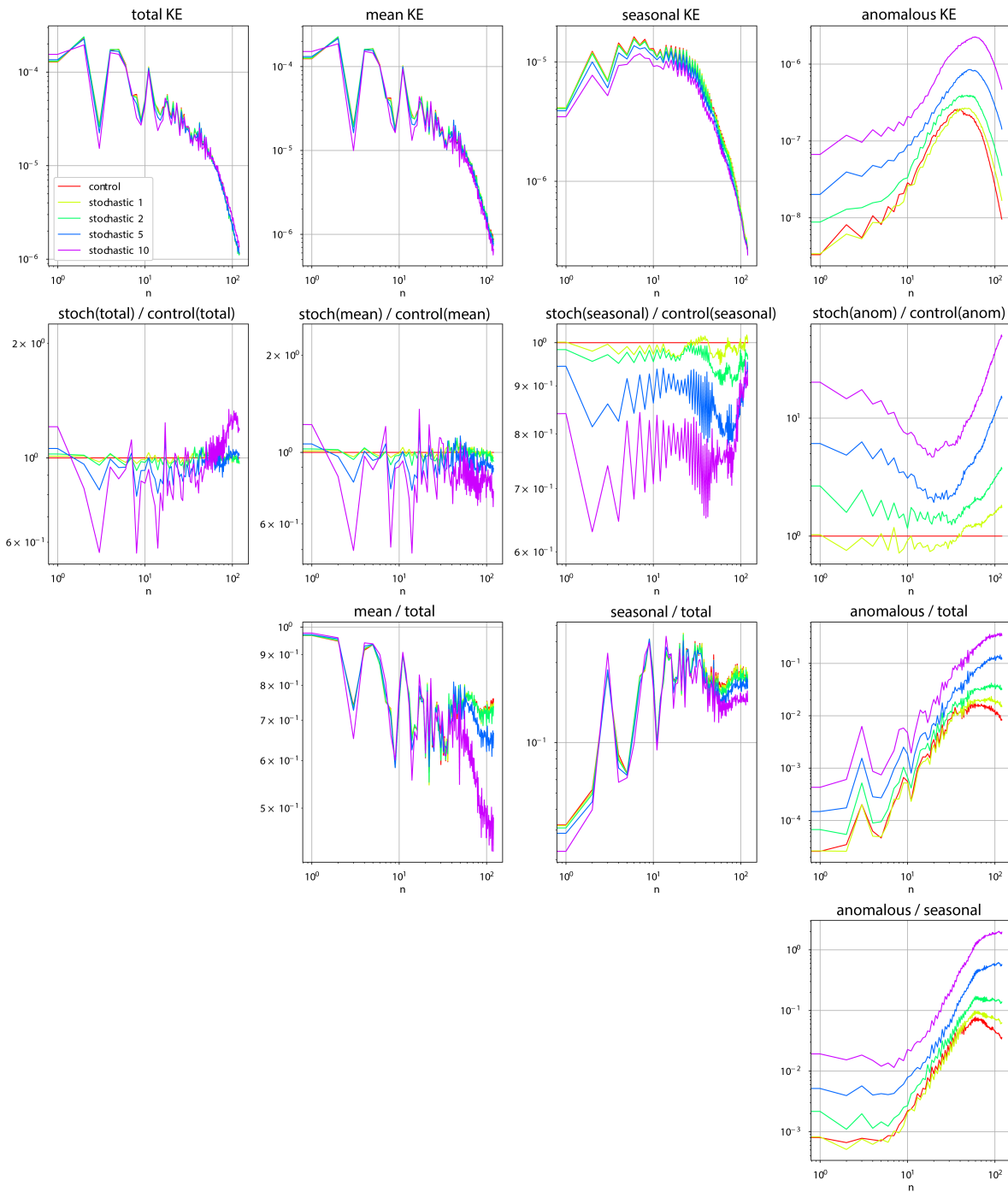
FIG. 3. Timeseries for globally summed KE, PE and temperature as annual averages.

278 forcing. The interesting result, is that as the forcing amplitude is increased energy is transferred
279 from the seasonal cycle (figure 4 top row third panel from the right) to generate transients (figure 4
280 top row last panel on the right) with transient KE being preferentially generated at the small scales
281 i.e. total wavenumbers $n \in [10, 100]$.

287 This observation is made even clearer when we consider the total, mean, seasonal and anomalous
288 KE as a ratio between forced and control simulations (figure 4 second row). For the ratio of
289 forced to control total, we see additional redistribution of KE from the large scales to the small
290 scales relative to the control as the stochastic forcing amplitude increases. In contrast, for the
291 mean and seasonal KE there is uniform transfer of KE to the transient anomalous KE across all
292 scales but in particular to the smallest resolved scales. This transfer to the transients exhibits a
293 cusp like functional form reminiscent of stochastic backscatter subgrid terms first described by
294 Kraichnan (1976) for homogeneous turbulent flows. Where we consider KE transfers from the
295 mean field to the transients at a given level (not shown) i.e. on a two-dimensional surface, the
296 results are directly interpretable in terms of the results of O’Kane and Frederiksen (2008b) (see
297 their figure 1 and figures 6c & d) and specifically momentum transfers due to the eddy-mean field
298 (nonlinear noise and dissipation terms) and eddy-topographic force. The transfers from the large
299 scale mean flow to generate small scale transients is even more clearly demonstrated when the
300 mean, seasonal and anomalous KE is normalised by the total KE at each wavenumber (figure 4 row
301 3). For scales smaller than total wavenumber $n = 50$, significant reductions in mean and seasonal
302 KE occur relative to the total KE for the stochastic-5 (50%) and stochastic-10 (100%) simulations.
303 For $n > 10$, this energy is preferentially redistributed to the smaller scales however some of the
304 mean and seasonal KE is uniformly transferred to the large scale structures i.e. $n \leq 10$. The extent
305 to which stochastic forcing initiates energy transfers from the seasonal to the transients is revealed
306 in the ratio of anomalous to seasonal KE (figure 4 bottom row).

307 3) TRANSIENT KINETIC ENERGY AND BAROCLINIC INSTABILITY

310 For a detailed examination of the energetics in physical space, we consider the transient kinetic
311 energy (Eq. 5) and potential energy transfer (Eq. 6) at each grid point for the surface averaged over
312 the last decade of the 170 year simulations. We first focus on the Southern Ocean and the ACC as a
313 representative region of high eddy variability (figure 5). As expected, the 0.1° reference calculation



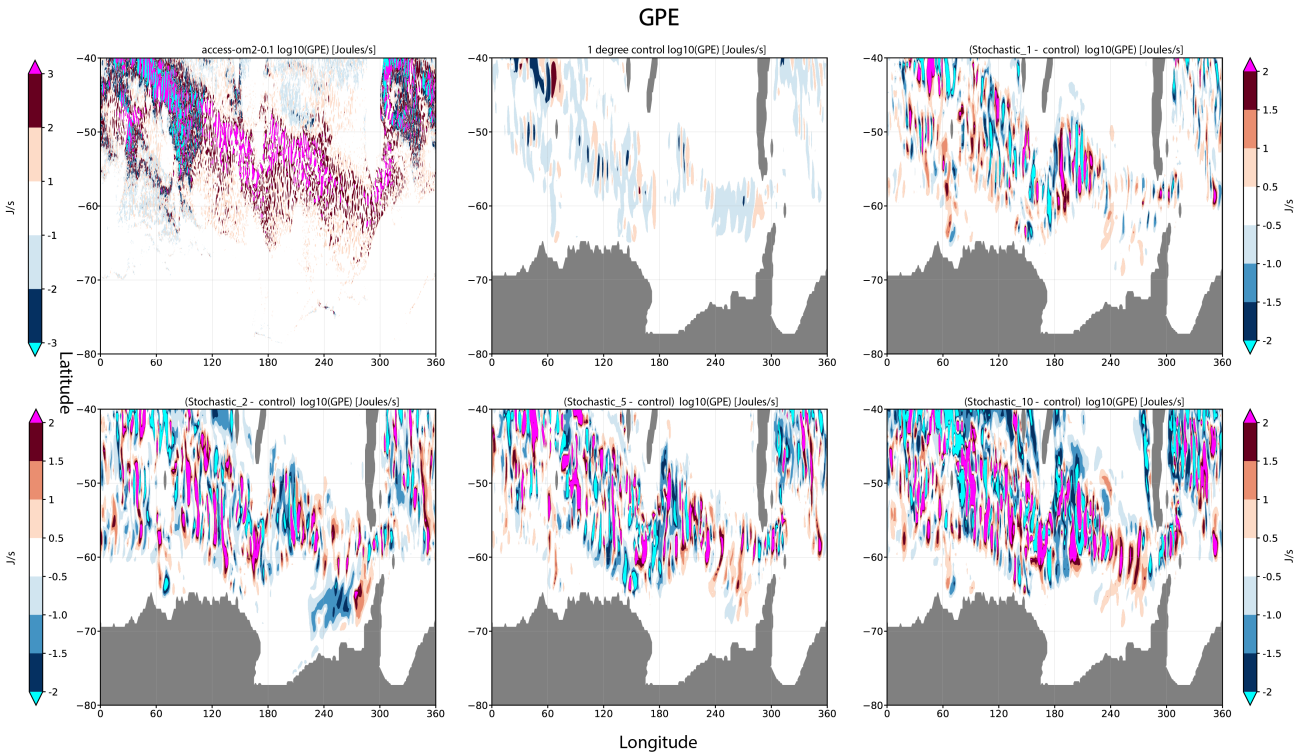
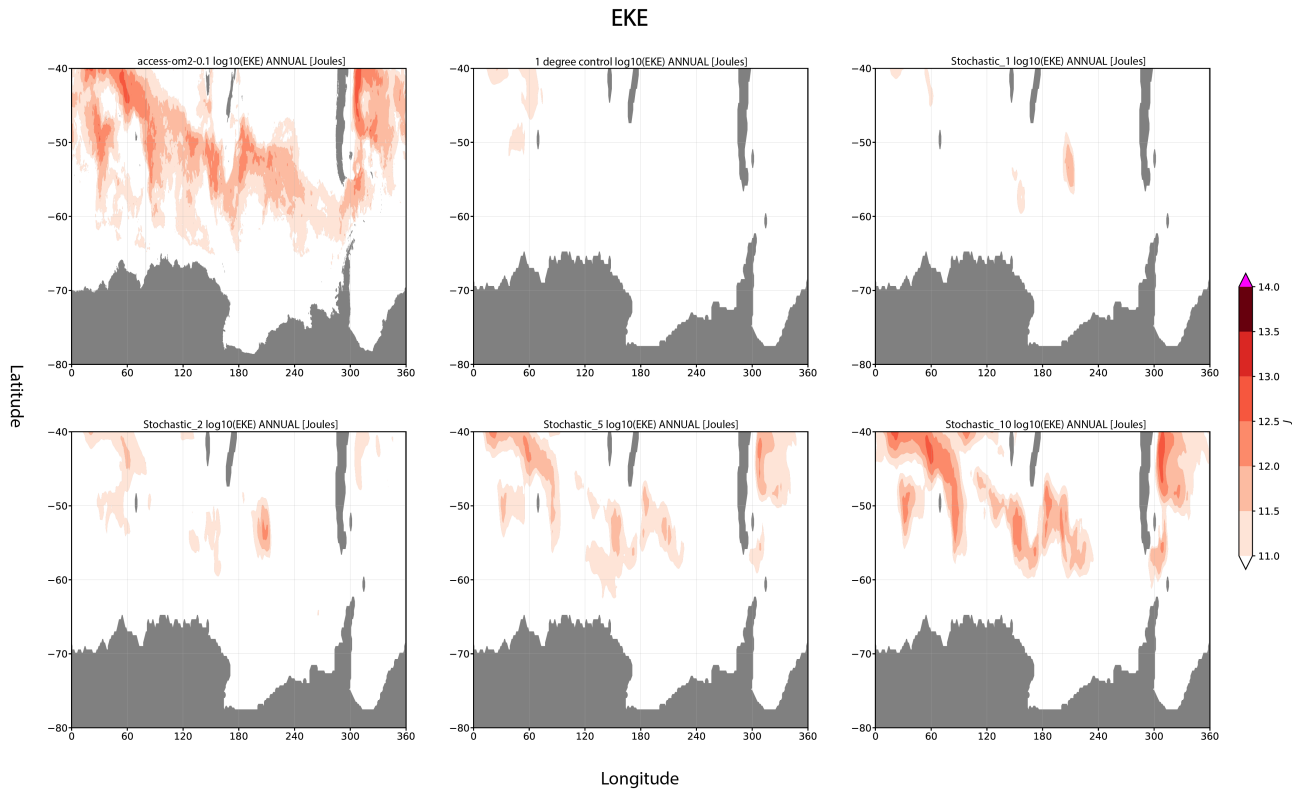
282 FIG. 4. Global KE spectra calculated from velocities depth averaged from 0-1000m for the 1° simulations.
 283 Shown in the top row are the total KE and the constituent terms of the triple-decomposition and in the second
 284 row as the ration of stochastically forced and control simulations. In row three we show the terms of the triple-
 285 decomposition normalised by the total KE and in the last row the ration of anomalous to seasonal KE for each of
 286 the 1° simulations.

314 show regions of high EKE throughout the ACC whereas for the 1° control simulation EKE is largely
315 absent. As the amplitude of the stochastic forcing increases so does EKE with initial responses co-
316 located about large topographic features. The stochastic-10 (100% amplitude) simulation displays
317 comparable values and spatial distributions of EKE to the 0.1° reference calculation.

318 Let us next consider baroclinic instability in the form of the transfer of mean to transient potential
319 energy (GPE). We again focus on the Southern Ocean and the January average over the last simulated
320 decade. In figure 5, the 0.1° reference calculation shows largely positive transfers in excess of
321 3 J/s between 120° - 300° E with more uniformly distributed structures with values in excess of
322 $\pm 3 \text{ J/s}$ elsewhere in the Atlantic and Indian ocean sectors. For the 1° control simulation, similar
323 meridionally oriented structures are present with typically much weaker values. With the addition
324 of even very weak stochastic forcing (stochastic-1 10%), structures with values comparable to the
325 0.1° reference calculation appear. These structures become larger in extent and magnitude as the
326 amplitude of the stochastic forcing increases and have previously been shown to be consistent with
327 Rossby waves which can also be excited by the addition of noise directly to the surface forcing
328 (O’Kane et al. 2013). O’Kane et al. (2014a) show that they, analogous to storm tracks in the mid-
329 latitude troposphere, are in fact higher order baroclinically unstable Rossby waves that propagate
330 within wave guides defined by potential density gradients in the subtropical and higher latitude
331 oceans.

332 In figure 6, we consider the zonal average GPE in the tropics, again for the January average over
333 the last simulated decade. The 1° control shows large-scale structures to 2000m in depth North of
334 10° N with values exceeding -4 J/s with lower values extending only to 1000m depth South of 10°
335 S. The values between $\pm 10^\circ$ latitude are small-scale and weak. With the application of stochastic
336 forcing, GPE values increase everywhere with larger scale structures appearing in the regions
337 poleward of 10° latitude and at greater depth in the South. For stochastic-5 (50%) forcing, GPE
338 values and structures in the equatorial regions closely match those of the 0.1° reference calculation.
339 As the latitude increases there are some structural differences between the 1° simulations and the
340 0.1° reference calculation, but with comparable values for the 50% and 100% forcing experiments.

341



308 FIG. 5. Southern Ocean anomalous KE averaged (EKE) and transfer rate of mean to anomalous PE (GPE) in
 309 the Southern Ocean averaged for January over last decade of simulations.

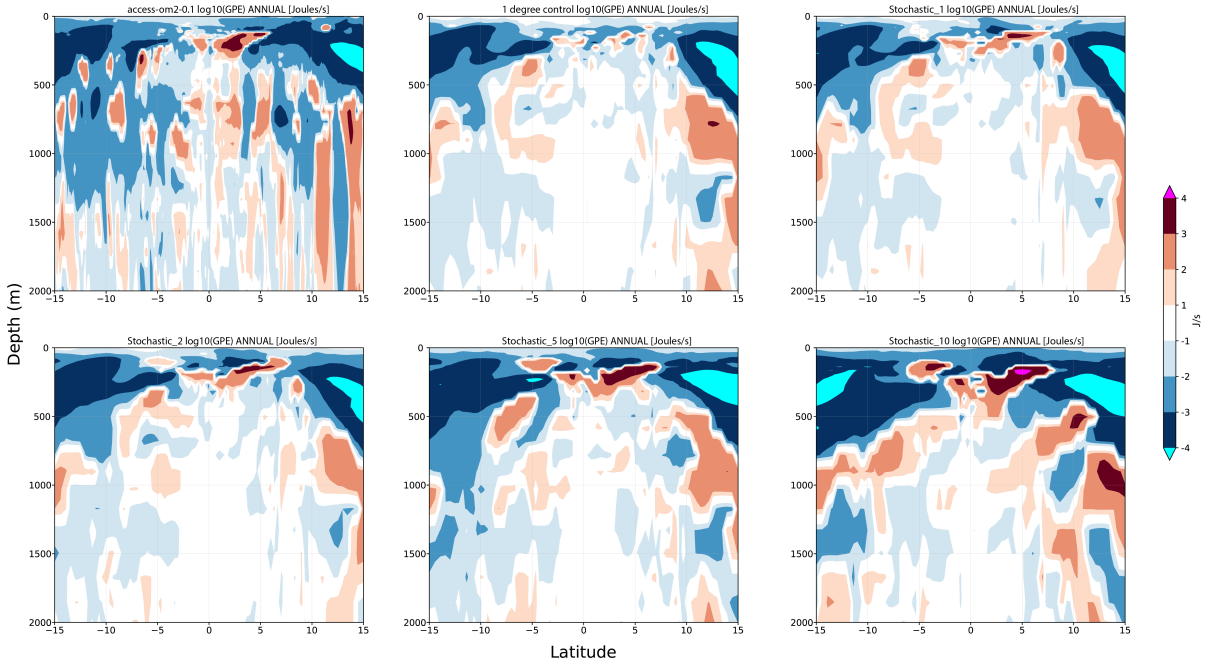
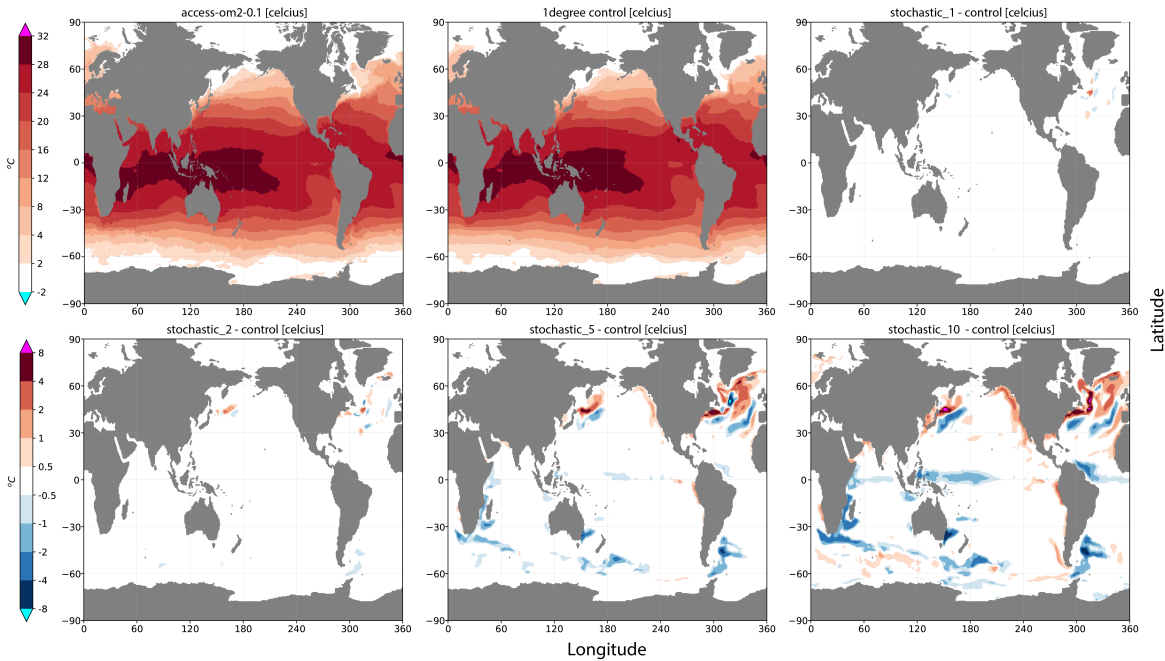


FIG. 6. Zonal average GPE in the tropics averaged for January over last decade of simulations.

342 *c. SST and MLD*

345 Given the observed transfer of energy from the mean and seasonal spectra to generate anomalous
 346 KE, the question arises as to the spatial imprint on the dynamically active regions. We begin
 347 by first comparing January SST climatologies for the low resolution control simulation, the high
 348 resolution reference calculation, and differences between the forced simulations and control (figure
 349 7). We first notice agreement between the high and low resolution simulations, in part expected
 350 due to the common surface boundary conditions but the general level of agreement is remarkable.
 351 With the application of stochastic forcing, we see the initial response in the mid-latitude boundary
 352 current regions of the North Pacific and Atlantic, once again notably in the regions associated with
 353 the Kuroshio extension and Gulf Stream separation.

356 For the stochastic-5 simulation, the Northern hemisphere responses are revealed as largely
 357 meridional displacements to the aforementioned boundary currents and in the Atlantic to the gyre
 358 circulation encompassing the North Atlantic drift and Canary current. In the western Pacific,
 359 we see warming along the Alaska and California currents. In the Southern hemisphere, there is
 360 cooling in the East Australian Current, the South Equatorial, Mozambique and Agulhas Currents,
 361 the Falklands Current and regions in the ACC.

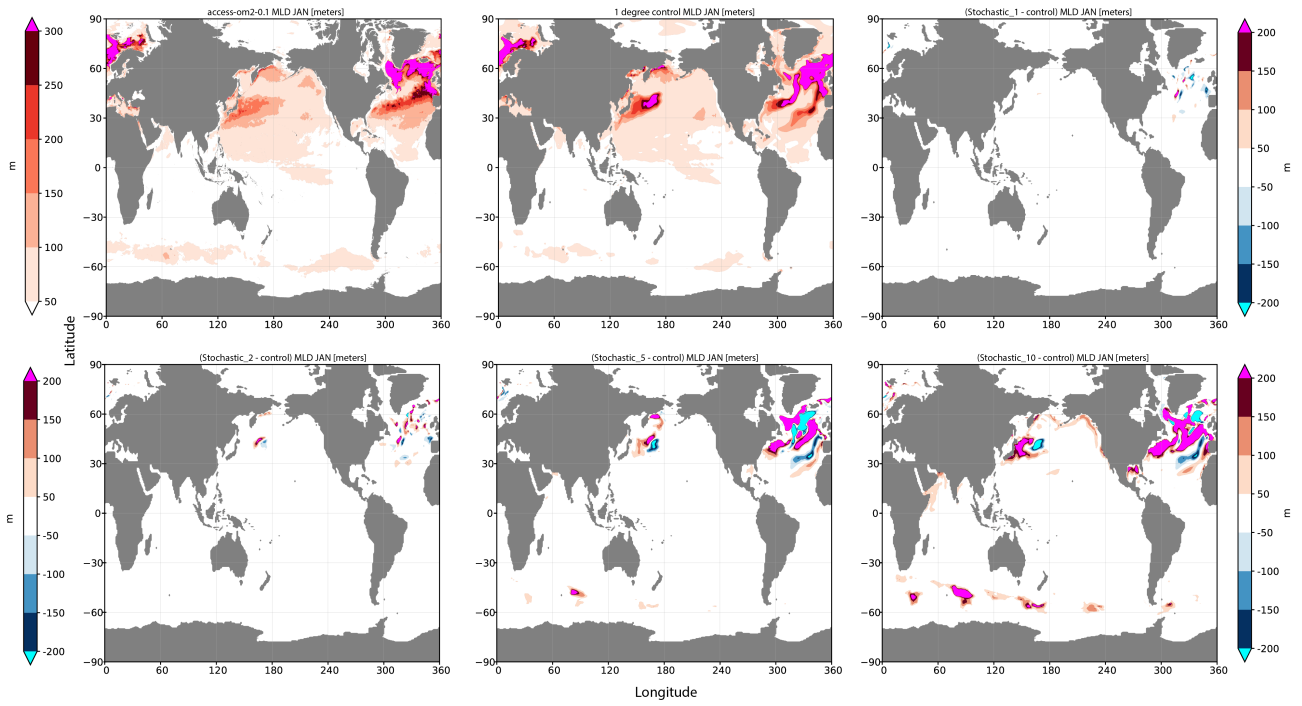


343 FIG. 7. High and low resolution reference calculations of SST and differences of stochastic forced w.r.t. control
 344 calculated for climatological January over the last decade of simulations.

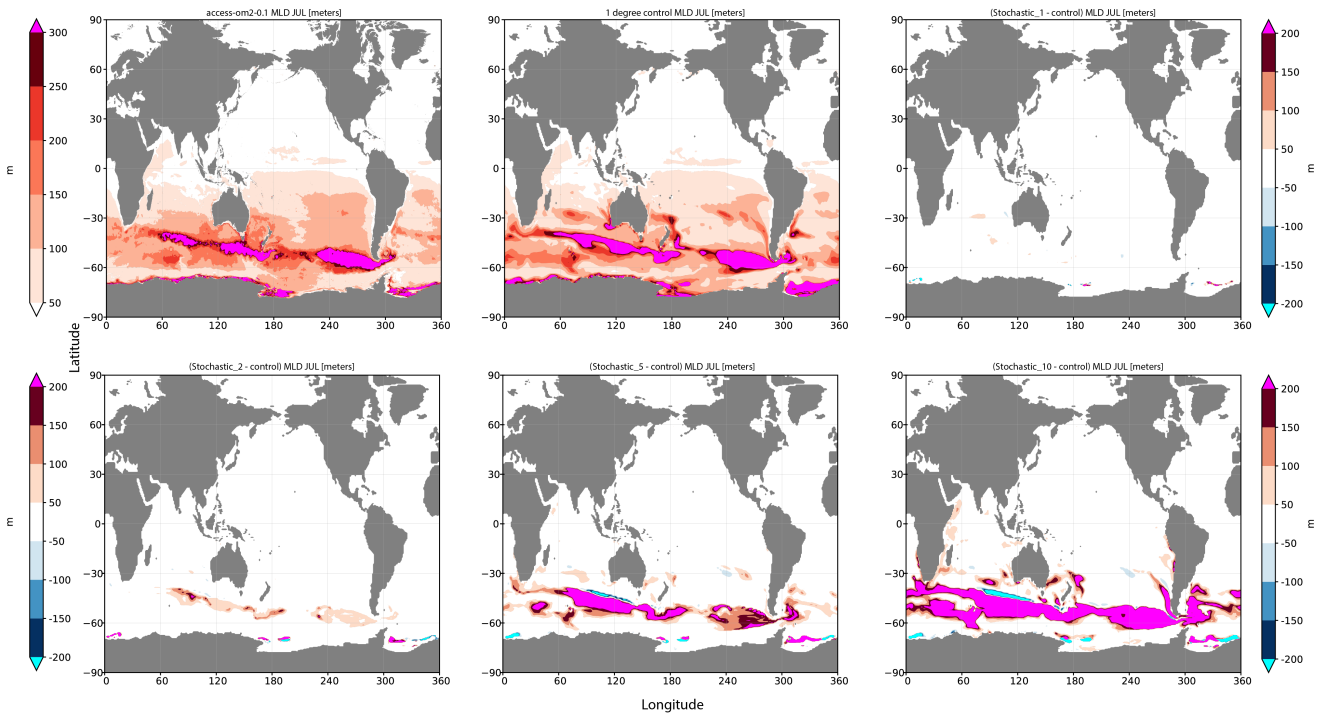
362 At 100% amplitude stochastic forcing (stochastic-10) there is further amplification of the afore-
 363 mentioned responses but with additional cooling in the western equatorial Pacific. In contrast to
 364 substantial cooling (up to 4°C) in the western equatorial Atlantic, warming is evident all along the
 365 Eastern coast of South America. The general patterns of warming and cooling in the Southern
 366 hemisphere are less representative of meridional displacement of currents and more indicative of
 367 changes to mixing processes. This is indeed shown to be the case in examination of the January
 368 climatological mixed layer depth (MLD) (figure 8). Of note is the substantial difference in MLD at
 369 the Kuroshio extension in the North Pacific at around 40°S between high resolution reference and
 370 low resolution control simulations. With increased forcing amplitudes, the meridional displace-
 371 ment of the currents in the Northern hemisphere are also shown to be accompanied by substantive
 372 changes in MLD. In the southern hemisphere, the cooling observed in the Southern Ocean is now
 373 revealed to occur primarily due to substantial increases in MLD of over 200m at locations where
 374 significant topographic features are located. This is indicative of increased momentum fluxes due
 375 to an enhancement of the eddy-topographic force. Considering the responses in July at the height
 376 of the austral winter (figure 8), substantive increases in MLD are observed throughout the ACC
 377 and, for maximum amplitude stochastic-10, at the Tasman Front extending from the Australian

MLD

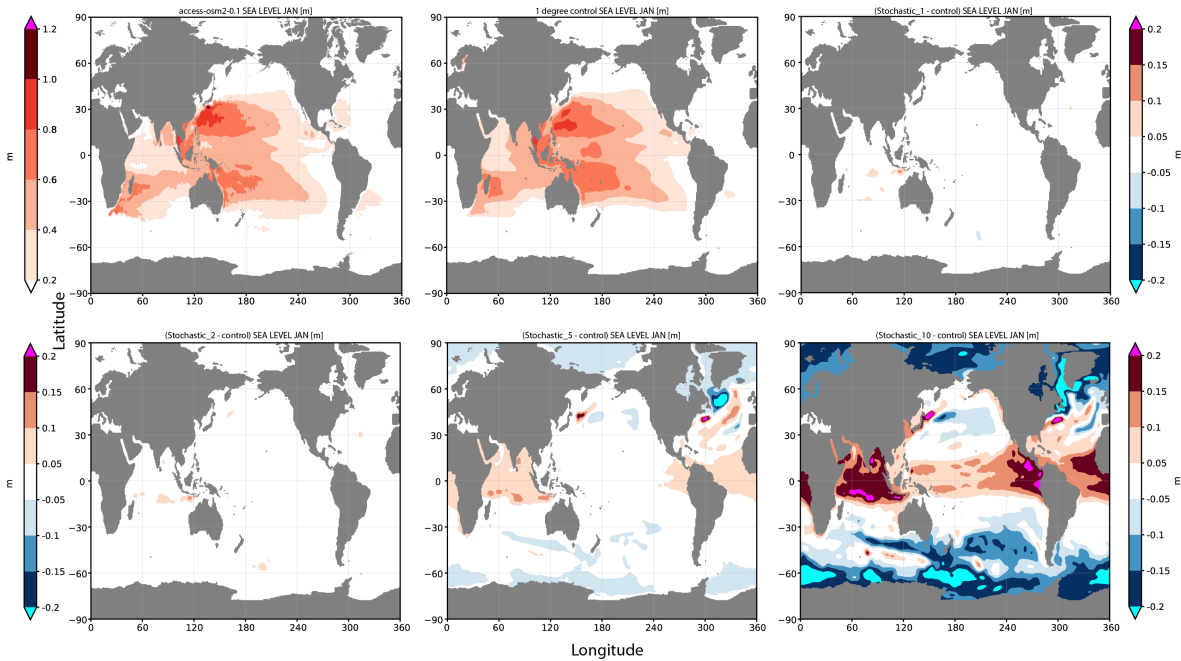
January



July



354 FIG. 8. High and low resolution reference calculations and differences of stochastic forced w.r.t. control
355 calculated over last decade of simulations for January and July averaged mixed layer depths.



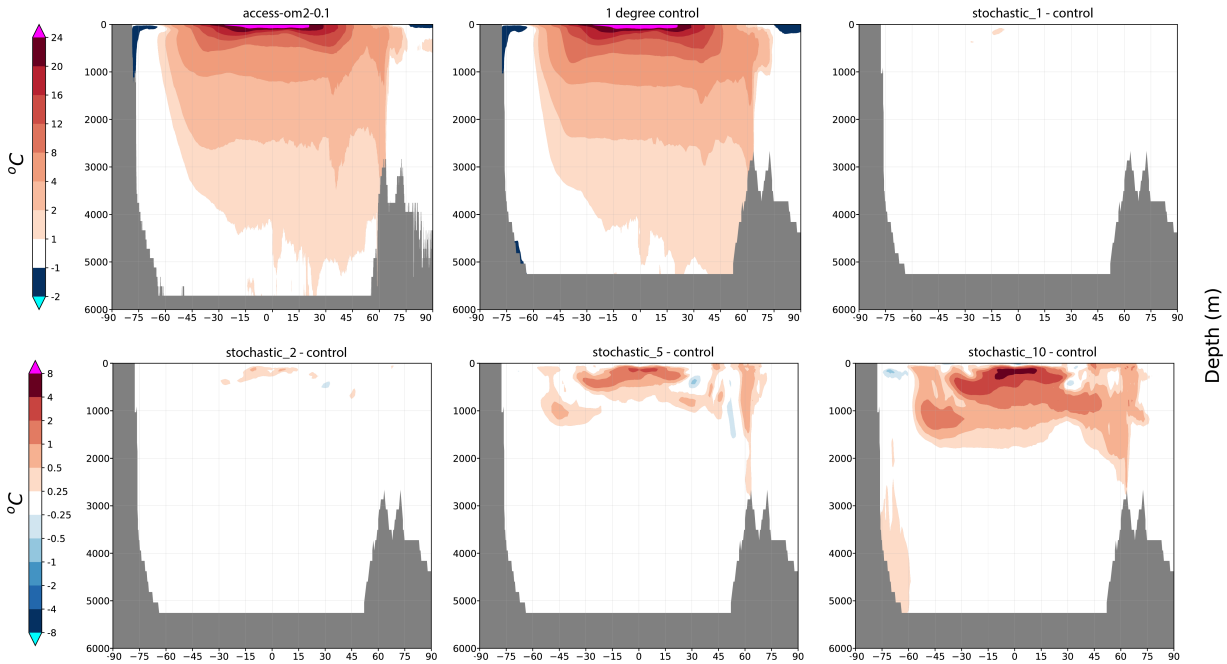
381 FIG. 9. High and low resolution reference calculations and differences of stochastic forced w.r.t. control
 382 calculated as a January climatological average over the last decade of simulations for sea level.

378 coast to the west of New Zealand and in the southern Atlantic in the region of the Brazil-Malvinas
 379 Confluence.

380 *d. Sea level, Temperature and OHC*

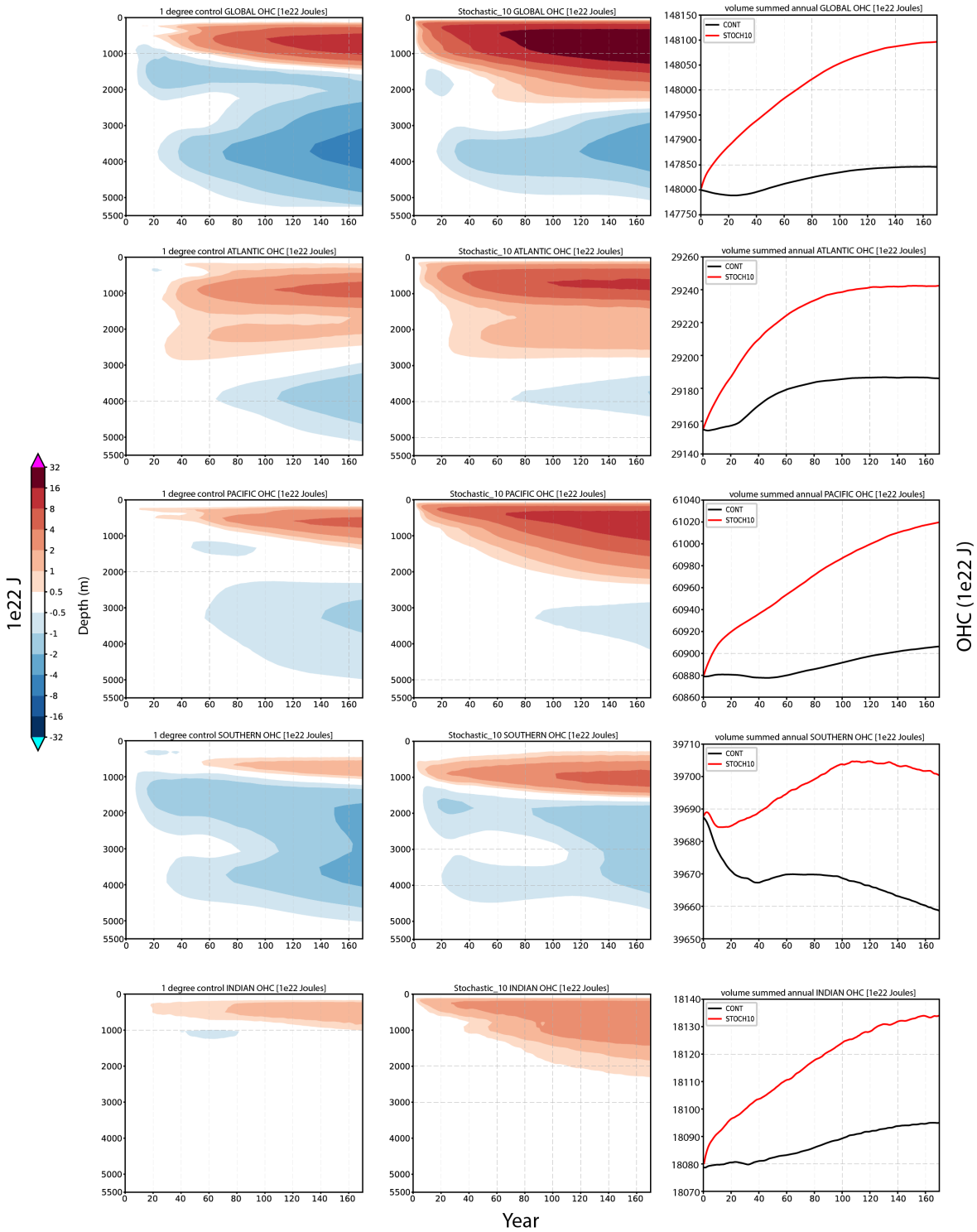
385 Regions of substantive surface cooling can also be accompanied by subduction of large amounts
 386 of heat and local increases in sea level. This is exactly the case where the surface cooling previously
 387 observed in the equatorial oceans for large amplitude stochastic forcing (figure 7) is shown to be
 388 associated with increases in sea level of over 20cm (figure 9 last panel) and anomalous temperature
 389 increases of more than 4 degrees at the thermocline (figure 10 last panel). Decreases in sea level
 390 occur in the mid-latitudes south of 30°S and at the high latitudes in the sea ice zones. These regions
 391 are however not associated with substantive surface (figure 7) or subsurface (figure 10) cooling
 392 rather, for the mid-latitude Southern Ocean, presumably occur due to increased mixing and an
 393 equatorward redistribution of heat to the tropics.

396 To better understand changes in sea level, we next consider ocean heat content (OHC) annually
 397 averaged globally and for the Atlantic, Pacific, Southern and Indian oceans through time, both
 398 integrated and by depth (figure 11), contrasting the 1° control and stochastic-10 simulations.



383 FIG. 10. High and low resolution reference calculations and differences of stochastic forced w.r.t. control
 384 calculated as a January climatological average over the last decade of simulations for zonal mean temperature.

389 The forced simulation requires around 150 years to reach a global steady state characterized by
 400 substantial increases in OHC at all depths but in particular above 2000m and, with accompanying
 401 increases in the mean thermocline depth from $\approx 1500\text{m}$ to $\approx 2500\text{m}$. While the change in global
 402 OHC is very small, representing an increase of only 0.17% globally, it is significant reaching around
 403 $100 \times 10^{22}\text{J}$ after 40 years before equilibrating at $250 \times 10^{22}\text{J}$ after 150 years. The change to OHC
 404 caused by strong uncorrelated transient (eddy) noise is of the same magnitude but opposite sign
 405 to that observed by Williams et al. (2016) employing strong correlated noise perturbations applied
 406 to the temperature tendencies. Where Williams et al. (2016) also observed warming in the top
 407 1000-2000m, they observed proportionally much larger cooling at depths between 3000-4000m, to
 408 the extent that there was a net cooling of the global ocean. In contrast, our results reveal warming
 409 at all depths with changes (units of $1e^{22}\text{J}$) in the Atlantic ≈ 55 , Southern ≈ 40 and Indian ≈ 40
 410 oceans at year 170, and where nearly half of the total warming occurs in the Pacific ≈ 115 , mostly
 411 concentrated at the equator (see also figure 10). In contrast to Williams et al. (2016), our results
 412 show no evidence of cooling at depth. As noted earlier, all our simulations have reached steady state
 413 for global OHC after a transient period of ≈ 150 years with no evidence of additional subduction
 414 of heat.



394 FIG. 11. Annually averaged ocean heat content (OHC) for the global, Atlantic, Pacific, southern and Indian
 395 oceans by depth and volume integrated . We show only the 1° control and stochastic-10 simulations.

415 *e. Transports*

416 Finally we are interested to see what impact the described changes in the climatological state have
417 on ocean transports (figure 12). We consider transports for Drake Passage, the Atlantic Meridional
418 Ocean Circulation at 26°N (AMOC26°N), Antarctic Bottom Water (AABW) and North Atlantic
419 Deep water (NADW). The methodology used in the calculation of these transports has been
420 described in detail in section 6d of O’Kane et al. (2021).

421 Drake Passage transport (figure 12) is a proxy for the strength of the ACC and is here calculated
422 using monthly averaged 3D ocean horizontal mass transports from which the eastward component
423 is integrated along a single line from the southern tip of South America to the northern tip of the
424 Antarctic Peninsula and to the ocean bottom. Here the ACC strength for the 0.1° high resolution
425 reference simulation lies on average between 140-150 Sv and between 150-160 Sv in the 1° control
426 increasing to a maximum of between 155-165 Sv for stochastic-10 with a near linear response to
427 increases in stochastic forcing amplitude. All simulations are within observational estimates of
428 the observed Drake Passage transport values which range between 134 ± 13 Sv (Whitworth and
429 Peterson 1985) and 173 Sv (Donohue et al. 2016).

430 The 0.1° high resolution reference transport for the AMOC cell is centered about the estimated
431 observed transport of 17.2 Sv at 26°N (McCarthy et al. 2015) and within the observed range of
432 seasonal variations between 10 and 25 Sv from the RAPID-WATCH (Smeed et al. 2015). However,
433 the 1° control reveals a much too weak AMOC26°N transport with seasonal fluctuations of between
434 3.5-9.5 Sv. Stochastic forcing acts to increase the transport by up to 3.75 Sv to maximum steady
435 state values of 12.5 Sv (stochastic-10). The 1° control NADW intensity averages between 7.5
436 -12 Sv whereas the high resolution reference ranges between 16-25 Sv. The stochastic-5 and
437 -10 simulations both generate seasonally varying values of between 10-15 Sv comparable to the
438 observed values ranging about ≈ 15 Sv (Lumpkin et al. 2008; Ganachaud 2003).

439 In the Southern Ocean, observed values of the AABW cell transports range from 5.6 ± 3.0 Sv
440 reported by Lumpkin and Speer (2007) to values of 9.77 ± 3.7 Sv reported in the Weddell Sea
441 (Sloyan and Rintoul 2001; Garabato et al. 2002; Talley 2013). In figure 12, the 0.1° high resolution
442 reference AABW transports lie within the range observed by Lumpkin and Speer (2007), whereas
443 the 1° control simulation values are much closer to those reported by Talley (2013) for example.

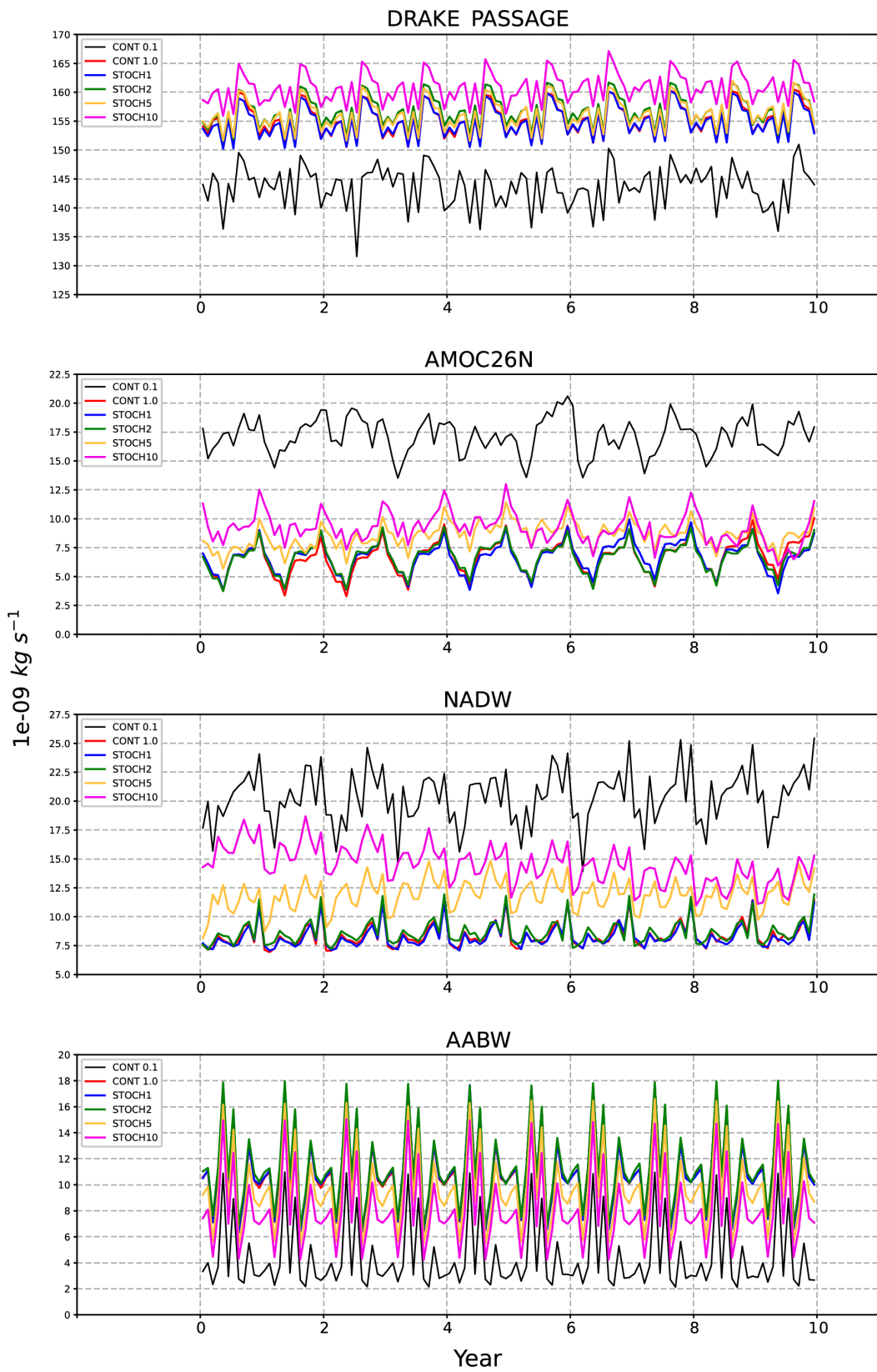


FIG. 12. Comparison of transports for Drake Passage, AMOC26°N, NADW and AABW.

444 Here the impact of increased noise is to reduce the average transport to be closer to the high
445 resolution reference values.

446 Thus, we see that the addition of noise is not to always increase transports, but, with the exception
447 of Drake Passage, to most often to make the dynamics of the low resolution non-eddy model
448 more consistent with that of the high resolution eddy model, whether that be to increase or
449 decrease volume transports. Apart from AABW, the 0.1° reference calculation transports display
450 less regular seasonal variability, despite having the same repeat forcing applied as the 1° degree
451 simulations. We ascribe this to the presence of randomly generated eddies with deep vertical extent
452 in the high resolution reference model but have not undertaken a rigorous examination of this point.

453 **4. Summary and Discussion**

454 Overall, we find implementation of a simple parameterization of ocean transients (eddies),
455 via stochastic perturbations to the horizontal momentum fluxes, leads to improvements in the
456 simulated climatological steady intrinsic ocean state. The statistics of the transients were calculated
457 from the velocities of a high-resolution, eddy-resolving ocean model ACCESS-OM2-0.1. After
458 thresholding, a three-dimensional mask was generated enabling the injection of stochastic noise
459 i.e., zero-mean random noise uniformly distributed between $[-1, 1]$, representative of subgrid
460 transients, into a low-resolution, 1° non-eddy-resolving variant of the same ocean - sea ice model
461 configuration. Four variants of the stochastically forced 1° ACCESS-OM2 model were considered,
462 with varying amplitudes of the noise relative to the high resolution reference calculation applied.
463 All low resolution model configurations were run to steady state before calculation of the statistics
464 of their respective climatological states.

465 Spectra from a triple-decomposition revealed that, despite having zero-mean, random noise
466 forcing was able initiate a redistribution of kinetic energy largely from seasonal variations to
467 generate large amplitude small scale anomalous transient kinetic energies. A major improvement
468 was observed in the energetics of the Southern Ocean where the transient kinetic energy of
469 the Antarctic Circumpolar Current, largely absent in the 1° control simulation, was able to be
470 approximated to large degree with amplitudes matching those simulated in the 0.1° reference
471 calculation for sufficiently strong stochastic forcing. Similar stochastic amplification was observed
472 in the transfer rate of mean to transient potential energy at all latitudes.

473 Surface temperature responses were largely consistent with increases in mixed layer depths
474 and meridional displacement of northern hemisphere boundary currents. Decreases in sea level
475 at the higher latitudes, compensated by increased sea levels at the equator, were found to be
476 largely in response to injection of heat into the equatorial Pacific at the thermocline and into the
477 mixed layer. While consistent warming was observed at all depths, by far the majority of the
478 OHC warming occurred in the equatorial Pacific upper ocean. Improvements in the transports
479 include important overturning circulations such as increases in strength of the AMOC_{26°N} and
480 NAWDW, and weakening of AABW. Only Drake Passage transport moved further from the high
481 resolution reference calculation but remained within the range of observational estimates. While
482 the maximum amplitudes of OHC differences between control and stochastic forcing experiments
483 were comparable to those observed by Williams et al. (2016) using perturbed temperature tendencies,
484 stochastic perturbations to the momentum fluxes produced global OHC warming whereas perturbed
485 temperature tendencies produced cooling of the total OHC. Both responses can be at least as large
486 in amplitude as the observed anthropogenic global warming signal.

487 Consistent with Williams et al. (2016) and the atmospheric study of Berner et al. (2012), we find
488 the addition of stochastic forcing can result in improvements comparable to significant increases
489 in horizontal resolution. We note that application of perturbations to the temperature tendencies
490 alone will be inconsistent with modifying the potential energy and inappropriate in regions of
491 density compensation, hence our motivation for modifying the momentum fluxes via the velocity
492 tendencies. Overall we advocate for oceanic stochastic parameterizations as a simple and effective
493 means to improve climate model simulations.

494 *Acknowledgments.* The authors acknowledge support from National Computational Infrastructure
495 (NCI) Australia. We also acknowledge the combined efforts of the Consortium for Ocean - Sea Ice
496 Modelling in Australia (COSIMA) in developing the model configurations used in this study.

497 *Data availability statement.* All model configurations are available from the COSIMA github
498 repository <https://github.com/COSIMA/access-om2>. The data and analysis codes are available on
499 request.

500 **References**

- 501 Andrejczuk, M., F. C. Cooper, S. Juricke, T. N. Palmer, A. Weisheimer, and L. Zanna, 2016:
502 Oceanic stochastic perturbations in a seasonal forecast system. *Mon. Wea. Rev.*, **144**, 1867–
503 1875, doi:10.1175/MWR-D-15-0245.1.
- 504 Beena, B. S., and J.-S. von Storch, 2009: Effects of fluctuating daily surface fluxes on the time-mean
505 oceanic circulation. *Clim. Dyn.*, **33**, 1–18, doi:10.1007/s00382-009-0575-y.
- 506 Berner, J., and coauthors, 2017: Stochastic parameterization: Toward a new view of weather and
507 climate models. *BAMS*, **25**, 565–587, doi:10.1175/BAMS-D-15-00268.1.
- 508 Berner, J., T. Jung, and T. N. Palmer, 2012: Systematic model error: The impact of increased
509 horizontal resolution versus improved stochastic and deterministic parameterizations. *J. Climate*,
510 **25**, 4946–4962, doi:10.1175/JCLI-D-11-00297.1.
- 511 Bouchet, F., and E. Simonnet, 2009: Random changes of flow topology in two-dimensional and
512 geophysical turbulence. *Physical Review Letters*, **109** (2), 094 504.
- 513 Chapman, C. C., B. M. Sloyan, T. J. O’Kane, and M. A. Chamberlain, 2020: Interannual subtropical
514 indian ocean variability due to long baroclinic planetary waves. *J. Climate*, **33**, 6765–6791, doi:
515 10.1175/JCLI-D-19-0469.1.
- 516 Donohue, K. A., K. L. Tracey, D. R. Watts, M. P. Chidichimo, and T. K. Chereskin, 2016: Mean
517 Antarctic Circumpolar Current transport measured in Drake Passage. *Geophysical Research*
518 *Letters*, **43**, 11 760–11 767, doi:10.1002/2016GL070319.
- 519 Epstein, E. S., 1969: Stochastic dynamic prediction. *Tellus*, **21**, 739–759.
- 520 Epstein, E. S., and E. J. Pitcher, 1972: Stochastic analysis of meteorological fields. *J. Atmos. Sci.*,
521 **29**, 244–257.
- 522 Fleming, R. J., 1971a: On stochastic dynamic prediction. I: The energetics of uncertainty and the
523 question of closure. *Mon. Wea. Rev.*, **99**, 851–872.
- 524 Fleming, R. J., 1971b: On stochastic dynamic prediction. II: Predictability and utility. *Mon. Wea.*
525 *Rev.*, **99**, 927–938.

- 526 Frankignoul, C., and K. Hasslemann, 1977: Stochastic climate models, Part II. Application
527 to sea-surface temperature anomalies and thermocline variability. *Tellus*, **29**, 289–305, doi:
528 10.3402/tellusa.v29i4.11362.
- 529 Franzke, C. L. E., T. J. O’Kane, J. Berner, P. D. Williams, and V. Lucarini, 2015: Stochastic climate
530 theory and modeling. *Wiley Interdiscip. Rev.: Climate Change*, **6**, 63–78, doi:10.1002/wcc.318.
- 531 Frederiksen, J. S., 1999: Subgrid-scale parameterizations of the eddy–topographic force, eddy
532 viscosity and stochastic backscatter for flow over topography. *J. Atmos. Sci.*, **56**, 1481–1494.
- 533 Ganachaud, A., 2003: Large-scale mass transports, water mass formation, and diffusivities esti-
534 mated from world ocean circulation experiment (WOCE) hydrographic data. *J. Geophys. Res.*,
535 **108**, doi:10.1029/2002JC001565.
- 536 Garabato, A. C. N., E. L. McDonagh, D. P. Stevens, K. J. Heywood, and R. J. Sanders, 2002:
537 On the export of Antarctic Bottom Water from the Weddell Sea. *Deep-Sea Research II*, **49**,
538 4715–4742.
- 539 Hasslemann, K., 1976: Stochastic climate models. Part i Theory. *Tellus*, **28A**, 473–485, doi:
540 10.1111/j.2153-3490.1976.tb00696.x.
- 541 Horenko, I., 2010: On the identification of nonstationary factor models and their application to
542 atmospheric data analysis. *J. Atmos. Sci.*, **67**, 1559–1574, doi:10.1175/2010JAS3271.1.
- 543 Hussain, A. K. M. F., and W. C. Reynolds, 1970: The mechanisms of an organised wave in a
544 turbulent shear flow. *J. Fluid Mech.*, **41**, 241–261.
- 545 Kalnay, E., 2003: *Atmospheric modeling, data assimilation and predictability*. Cambridge Univer-
546 sity Press.
- 547 Kiss, A. E., and Coauthors, 2020: ACCESS-OM2 v1.0: a global ocean–sea ice model at three
548 resolutions. *Geosci. Model Dev.*, **13**, 401–442, doi:10.5194/gmd-13-401-2020.
- 549 Kitsios, V., L. Cordier, J. P. Bonnet, A. Ooi, and J. Soria, 2010: Development of a nonlinear
550 eddy-viscosity closure for the triple-decomposition stability analysis of a turbulent channel. *J.*
551 *Fluid Mech.*, **664**, 74–107, doi:10.1017/S0022112010003617.

- 552 Kitsios, V., J. S. Frederiksen, and M. J. Zidikheri, 2016: Theoretical comparison of subgrid turbu-
553 lence in atmospheric and oceanic quasi-geostrophic models. *Nonlinear Processes in Geophysics*,
554 **23**, 95–105.
- 555 Kraichnan, R., 1976: Eddy viscosity in two and three dimensions. *J. Atmos. Sci.*, **33**, 1521–1536.
- 556 Lou, J., T. J. O’Kane, and N. J. Holbrook, 2021: A linear inverse model of tropical and south
557 pacific climate variability: Optimal structure and stochastic forcing. *J. Climate*, **34**, 143–155,
558 doi:10.1175/JCLI-D-19-0964.1.
- 559 Loxley, P. N., and B. T. Nadiga, 2013: Bistability and hysteresis of maximum-entropy states in
560 decaying two-dimensional turbulence. *Physics of Fluids*, **25** (1), 015 113.
- 561 Lumpkin, R., and K. Speer, 2007: Global ocean meridional overturning. *J. Phys. Oceanogr.*, **37**,
562 2550–2562.
- 563 Lumpkin, R., K. Speer, and K. Koltermann, 2008: Transport across 48°N in the Atlantic Ocean. *J.*
564 *Phys. Oceanogr.*, **38**, 733–752.
- 565 Madec, G., and the NEMO team, 2016: *NEMO ocean engine*. Note du Pôle de modélisation, Institut
566 Pierre-Simon Laplace (IPSL) No 27, ISSN No 1288-1619, URL [https://www.nemo-ocean.eu/
567 doc/](https://www.nemo-ocean.eu/doc/).
- 568 McCarthy, G., and Coauthors, 2015: Measuring the Atlantic meridional overturning circulation at
569 26°N. *Progress in Oceanography*, **130**, 91–111, doi:10.1016/j.pocean.2014.10.006.
- 570 Metzner, P., L. Putzig, and I. Horenko, 2012: Analysis of persistent nonstationary time series and
571 applications. *Comm. App. Math. Comp. Sci.*, **7**, 175–229, doi:10.2140/camcos.2012.7.175.
- 572 Miller, R. N., M. Ghil, and F. Gauthiez, 1985: Data assimilation in strongly nonlinear systems. *J.*
573 *Atmos. Sci.*, **51**, 1037–1056.
- 574 Nadiga, B. T., and T. J. O’Kane, 2017: Nonlinear and stochastic climate dynamics. *Low-frequency*
575 *regime transitions and predictability of regimes in a barotropic model*, C. L. E. Franzke, and T. J.
576 O’Kane, Eds., Cambridge University Press, chap. 5, 136–158, doi:10.1017/9781316339251.
- 577 Oey, L. Y., 2007: Loop current and deep eddies. *J. Phys. Oceanogr.*, **38**, 1426–1449, doi:10.1175/
578 2007JPO3818.1.

- 579 O’Kane, T. J., and J. S. Frederiksen, 2008a: A comparison of statistical dynamical and ensemble
580 prediction methods during blocking. *J. Atmos. Sci.*, **65**, 426–447, doi:10.1175/2007JAS2300.1.
- 581 O’Kane, T. J., and J. S. Frederiksen, 2008b: Statistical dynamical subgrid-scale parameterizations
582 for geophysical flows. *Physica Scripta*, **T132**, 014 033.
- 583 O’Kane, T. J., R. J. Matear, M. A. Chamberlain, and P. R. Oke, 2014b: ENSO regimes and the late
584 1970’s climate shift: The role of synoptic weather and South Pacific ocean spiciness. *J. Comp.
585 Phys.*, **271**, 19–38, doi:10.1016/j.jcp.2013.10.058.
- 586 O’Kane, T. J., R. J. Matear, J. S. Risbey, B. M. Sloyan, and I. Horenko, 2013: Decadal variability
587 in an OGCM Southern Ocean: Intrinsic modes, forced modes and metastable states. *Ocean
588 Modelling*, **69**, 1–21, doi:10.1016/j.ocemod.2013.04.009.
- 589 Oliver, E. C. J., T. J. O’Kane, and N. J. Holbrook, 2015: Projected changes to tasman sea eddies
590 in a future climate. *J. Geophys. Res. Oceans*, **120**, 1–16, doi:10.1002/2015JC010993.
- 591 Orlandi, I., and M. D. Cox, 1973: Baroclinic instability in ocean currents. *Geophys. Fluid Dyn.*,
592 **4**, 297–332.
- 593 O’Kane, T. J., R. J. Matear, M. A. Chamberlain, E. C. J. Oliver, and N. J. Holbrook, 2014a: Storm
594 tracks in the southern hemisphere subtropical oceans. *J. Geophys. Res. Oceans*, **119**, 6078–6100,
595 doi:10.1002/2014JC009990.
- 596 O’Kane, T. J., P. R. Oke, and P. A. Sandery, 2011: Predicting the East Australian Current. *Ocean
597 Modelling*, **38**, 251–266, doi:10.1016/j.ocemod.2011.04.003.
- 598 O’Kane, T. J., and Coauthors, 2021: Cafe60v1: A 60-year large ensemble climate reanalysis. Part
599 II: Evaluation. *J. Climate*, **34**, 1571–1594.
- 600 Penland, C., 1989: Random forcing and forecasting using principal oscillation pattern analysis.
601 *Mon. Wea. Rev.*, **117**, 2165–2185, doi:10.1175/1520-0493(1989)117,2165:RFAFUP.2.0.CO;2.
- 602 Penland, C., and P. D. Sardeshmukh, 1995: The optimal growth of tropical sea surface temperature
603 anomalies. *J. Climate*, **8**, 1999–2024, doi:10.1175/1520-0442(1995)008,1999:TOGOTS.2.0.
604 CO;2.

605 Pitcher, E. J., 1977: Application of stochastic dynamic prediction to real data. *J. Atmos. Sci.*, **34**,
606 3–21.

607 Quinn, C., D. Harries, and T. J. O’Kane, 2021: Dynamical analysis of a reduced model for the
608 north atlantic oscillation. *J. Atmos. Sci.*, **78**, 1671, doi:10.1175/JAS-D-20-0282.1.

609 Sloyan, B. M., and S. R. Rintoul, 2001: The Southern Ocean limb of the global deep overturning
610 circulation. *J. Phys. Oceanogr.*, **31**, 143–173.

611 Smeed, D., G. McCarthy, D. Rayner, B. I. Moat, W. E. Johns, M. O. Baringer, and C. S. Meinen,
612 2015: Atlantic meridional overturning circulation observed by the RAPID-MOCHA-WBTS
613 (RAPID-Meridional Overturning Circulation and heatflux array-western boundary time series)
614 array at 26N from 2004 to 2014. *British Oceanographic Data Centre - Natural Environment*
615 *Research Council*, doi:10/6qb.

616 Stewart, K., and Coauthors, 2020: JRA55-do-based repeat year forcing datasets for driving
617 ocean–sea-ice models. *Ocean Modelling*, **147**, 101 557, doi:10.1016/j.ocemod.2019.101557.

618 Talley, L. D., 2013: Closure of the global overturning circulation through the Indian, Pacific, and
619 Southern Oceans: Schematics and transports. *Oceanography*, **26**, 80–97, doi:10.5670/oceanog.
620 2013.07.

621 Whitworth, T., and R. Peterson, 1985: Volume transport of the Antarctic Circumpolar Current
622 from bottom pressure measurements. *J. Phys. Oceanogr.*, **15**, 810–816.

623 Williams, P. D., 2012: Climatic impacts of stochastic fluctuations in air-sea fluxes. *Geophys. Res.*
624 *Lett.*, **39**, L10 705, doi:10.1029/2012GL051813.

625 Williams, P. D., N. J. Howe, J. M. Gregory, R. S. Smith, and M. J. Joshi, 2016: Improved climate
626 simulations through a stochastic parameterization of ocean eddies. *J. Climate*, **29**, 8763–8781,
627 doi:10.1175/JCLI-D-15-0746.1.

628 Zavala-Garay, J., A. M. Moore, C. L. Perez, and R. Kleeman, 2003: The response of a coupled
629 model of ENSO to observed estimates of stochastic forcing. *J. Climate*, **16**, 2827–2842.

630 Zhou, Y., 2021: Turbulence theories and statistical closure approaches. *Physics Reports*, **935**,
631 1–117, doi:10.1016/j.physrep.2021.07.001.

632 Zidiheri, M., and J. S. Frederiksen, 2008: Stochastic subgrid-scale modelling for non-equilibrium
633 geophysical flows. *Philos. Trans. Roy. Soc. London*, **36A**, 145–160, doi:10.1098/rsta.2009.0192.